Energy & Environmental Science

PAPER

View Article Online
View Journal | View Issue

Cite this: *Energy Environ. Sci.*, 2019, **12**, 988

Helical cobalt borophosphates to master durable overall water-splitting†

Prashanth W. Menezes,*[a] Arindam Indra,[a] Ivelina Zaharieva,*[b] Carsten Walter,[a] Stefan Loos,[b] Stefan Hoffmann,[a] Robert Schlögl,[c] Holger Dau*[b] and Matthias Driess*[a]

Received 8th June 2018,
Accepted 17th October 2018

DOI: 10.1039/c8ee01669k

rsc.li/ees

The sustainable electrochemical production of hydrogen from water is a key element in the transition toward carbon-neutral energy systems. Application at a global scale requires the discovery of precious metal-free electrocatalysts that unify high energetic efficiency, long-term stability and economic viability. Here we report the striking properties of noble metal-free, alkali-metal cobalt borophosphates acting as robust and efficient materials for bi-functional electrocatalytic water-splitting to give hydrogen and oxygen. Alkali-metal cobalt borophosphates are porous crystalline inorganic materials with chiral DNA-like helical structures bearing two chemically distinct types of water molecules, coordinated and strands of hydrate water associated *via* hydrogen bonds, located in the channels, which are predestined to possess superior catalytic performance. Depending on the applied electrode potential, they can be reversibly switched between catalysis of the hydrogen and oxygen evolution reactions, both at low overpotentials. This bifunctionality provides access to technologically simple overall water-splitting systems with energetic efficiencies exceeding the 75% level (above 90% based on a higher heating value) and uncompromised long-term stability, now verified with a two-and-a-half month period.

Broader context

The detrimental effect of combustion of fossil fuels to produce energy can be avoided by the implementation of renewable energy sources. In this regard, electrochemical water-splitting has been considered as an attractive strategy to generate clean and renewable energy, which comprises the hydrogen evolution reaction (HER) at the cathode and the oxygen evolution reaction at the anode (OER) to form molecular hydrogen and oxygen, respectively. Today, commercial electrolyzers to split water are operated at 1.8–2.0 V, substantially greater than the theoretical value of 1.23 V. Apart from the operational voltage, the long-lasting stability is a matter of great concern. Therefore, designing efficient, durable and robust multifunctional electrocatalyst systems to enhance water-splitting performance is highly desirable yet a prodigious challenge. At the same time, understanding the mechanism of water-splitting and describing the structure of the active catalyst is also crucial for the further development of this field. Here, we introduce borophosphates, a new class of chiral materials based on a transition metal for efficient and durable electrochemical water-splitting. Borophosphates are known for their captivating crystal chemistry with diverse structural architectures. Unexpectedly, this system can produce hydrogen and oxygen for months (at 1.53 V) under alkaline electrochemical conditions, thus offering a cost-effective and suitable earth abundant material system for practical implementation. We further describe the active catalyst structure during hydrogen and oxygen evolution and correlate the structure with the activity of the catalysts.

Introduction

With decreasing resources of fossil fuels and a rising demand for growth of a sustainable energy economy without net CO_2 emissions, it is essential to utilize renewable energy more effectively for production of non-fossil fuels.[1–4] One attractive way is the formation of hydrogen (H_2) and oxygen (O_2) through efficient and sustainable electrolysis of water.[5] Use of novel low-overpotential and bi-functional catalyst materials for both the H_2 evolution reaction (HER) and the O_2 evolution reaction (OER) in a common reaction medium could make the complete system more energy efficient and robust for practical applications.[6–9]

[a] *Department of Chemistry: Metalorganics and Inorganic Materials, Technische Universität Berlin, Straße des 17 Juni 135, Sekr. C2, 10623 Berlin, Germany. E-mail: matthias.driess@tu-berlin.de, prashanth.menezes@mailbox.tu-berlin.de*
[b] *Fachbereich Physik, Freie Universität Berlin, Arnimallee 14, 14195 Berlin, Germany. E-mail: holger.dau@fu-berlin.de, ivelina.zaharieva@fu-berlin.de*
[c] *Fritz Haber Institute of the Max Planck Society, Faradayweg 4–6, 14195 Berlin, Germany*

† Electronic supplementary information (ESI) available: Characterization and structural details, the electrochemical activity measurements, and the microscopic, spectroscopic and analytical details of the catalysts. See DOI: 10.1039/c8ee01669k

Noble metal-based materials have shown promising catalytic activity for either the OER (ruthenium, iridium) or the HER (platinum), but scarcity and high costs remain a major impediment for their pervasive use.[10,11] Pronounced progress has been achieved in the last few years in developing noble metal-free derived catalysts, especially with earth-abundant transition metals (TMs) for the OER and HER.[12–18] Moreover, apart from attaining higher catalytic activity, special efforts have also been dedicated to the realization of long-term stable catalytic systems.[19–21] Current technological systems for alkaline water electrolysis are often based on (initially) metallic nickel electrodes at the anode and the cathode that act as bifunctional catalysts for both the OER and HER. In spite of tremendous efforts dedicated to this perplexing area, a bifunctional, noble-metal free HER and OER catalyst that excels with high current densities at low overpotentials and is robust so that it can rival the performance of metallic nickel electrodes is still far from reality.[22] Bifunctional electrodes with the same catalyst material for both the HER and OER could be beneficial with respect to their ease of production and applicability, *e.g.*, single-step deposition of both catalysts by coating of anodes and cathodes in integrated systems for light-driven water-splitting. Unexpected progress along this line is reported herein.

Phosphates have attracted tremendous interest for the OER since the discovery of *in situ* deposited cobalt interlayer (oxide) phosphate by Nocera and co-workers and the curiosity on such amorphous interlayer cobalt phosphate (including crystalline phosphate) materials has grown comprehensively over the past few years.[23–31] Interestingly, Artero and co-workers were able to synthesize recently a Janus cobalt-based electrocatalyst which forms metallic cobalt coated with a cobalt-oxo/hydroxo-phosphate layer to mediate the HER and switches to catalyze the OER under anodic conditions.[32] On the other hand, borates are known for their manifold structural chemistry and gained much attention when Nocera and co-workers reported a nickel borate for the OER under near-neutral pH conditions.[33] Sizeable importance has been given to the development of nickel or cobalt borate films as OER catalysts in neutral conditions in the last couple of years but achieving enhanced activity with them is extremely challenging.[34–36]

In contrast, borophosphates (BPOs), intermediate compounds of M_xO_y–B_2O_3–P_2O_5–(H_2O) systems (M = main group or TM), were considered to inherit catalytic properties that are usually impossible to possess by either borate or phosphate alone.[37] Theoretical studies have also predicted that BPOs have high specific energies and energy densities in the electrolyte stability window and should be potential candidates for promising electrochemical applications.[38] BPOs are known for their rich structural chemistry and contain complex anionic structures built of interconnected trigonal–planar BO_3 and/or BO_4 and PO_4 groups and their partially protonated species (Fig. S1 and S2, ESI†).[37,39] The structural chemistry of BPOs is based on the linking principles of primary building units following the general line of silicate structural chemistry, which are classified on the basis of dimensionality *vs.* molar B : P ratios of their anionic partial structure (Fig. S2, ESI†).[40] The construction of complex BPO anions comprises isolated species, oligomers, rings, chains, layers and even 3D frameworks.[40] Keeping this in mind, we aimed to explore a novel class of materials, *i.e.*, two helical borophosphates $LiCo(H_2O)_2[BP_2O_8]\cdot H_2O$ (**LiCoBPO**) and $NaCo(H_2O)_2[BP_2O_8]\cdot H_2O$ (**NaCoBPO**) for electrocatalytic overall water-splitting. We discovered that these materials are not only switchable bifunctional catalysts in the HER and OER but also combine outstanding performance and energetic efficiency with high durability (> 2.5 months) in alkaline water electrolysis. This and the structure–activity relationships of the materials, the nature of active species involved and the surface-structural arrangements in each half reaction are here reported.

Results and discussion

Structural analysis

Single crystals of both **LiCoBPO** and **NaCoBPO** are accessible by a mild hydrothermal technique (see Experimental). The phase purity of the products was proven by Rietveld refinement of the powder X-ray diffraction pattern (PXRD), and the corresponding lattice parameters of a hexagonal cell were determined to be a = 9.4392(5) Å and c = 15.7255(8) Å for **LiCoBPO** and a = 9.4601(14) Å and c = 15.8430(2) Å for **NaCoBPO** that are consistent with the single crystal structure refinements (Fig. S3, ESI†).[41] Optical and scanning electron microscopy (SEM) showed that the deep pink crystals have a hexagonal bipyramidal shape (Fig. 1a and Fig. S4, S5, ESI†) and are porous (Fig. 1b and Fig. S6, ESI†). Transmission electron microscopy (TEM) displayed preservation in morphology (Fig. S7, ESI†) and the composition of materials was confirmed by inductively coupled plasma atomic emission spectroscopy (ICP-AES) and energy dispersive X-ray (EDX) analysis (Fig. S8 and Table S1, ESI†). Furthermore, the presence of ligated as well as crystal water was determined by Fourier transform infrared (FT-IR) spectroscopy (Fig. S9, ESI†). Notably, the flexibility of the helices through dehydration was monitored by thermogravimetric analysis (TGA) and its differential (DTG) (Fig. S10, ESI†). The chemical state, bonding situation and surface structure of the BPO single crystals were analyzed by X-ray photoelectron spectroscopy (XPS; and Fig. S11 and S12, ESI†).

The helical BPOs crystallize in the chiral space groups $P6_522$ and $P6_122$, respectively. The main structural features are one-dimensional infinite loop-branched helical $^1_\infty[BP_2O_8]^{3-}$ chains built of alternating borate and phosphate tetrahedra connected *via* common corners. The arrangement around a six-fold screw axis forms helices which are ''left-handed'' (6_5) or ''right-handed'' (6_1) (Fig. 1c).[41] This fascinating chiral arrangement of tetrahedral building units is similar to α-quartz (SiO_2) with 3_1 and 3_2 screw axes.[42] The structure can also be compared with the molecule deoxyribonucleic acid (DNA), where double-strands form a helical structure and the handedness of DNA can be determined from the twisting direction of the two strands.[43] The helices $^1_\infty[BP_2O_8]^{3-}$ running along [001] are interconnected *via* $CoO_4(OH_2)_2$ coordination octahedra, and the free threads of helices are occupied by lithium or sodium ions which are in an irregular surrounding of oxygen atoms (Fig. 1d).[44] The remaining crystal waters form hydrogen bonds

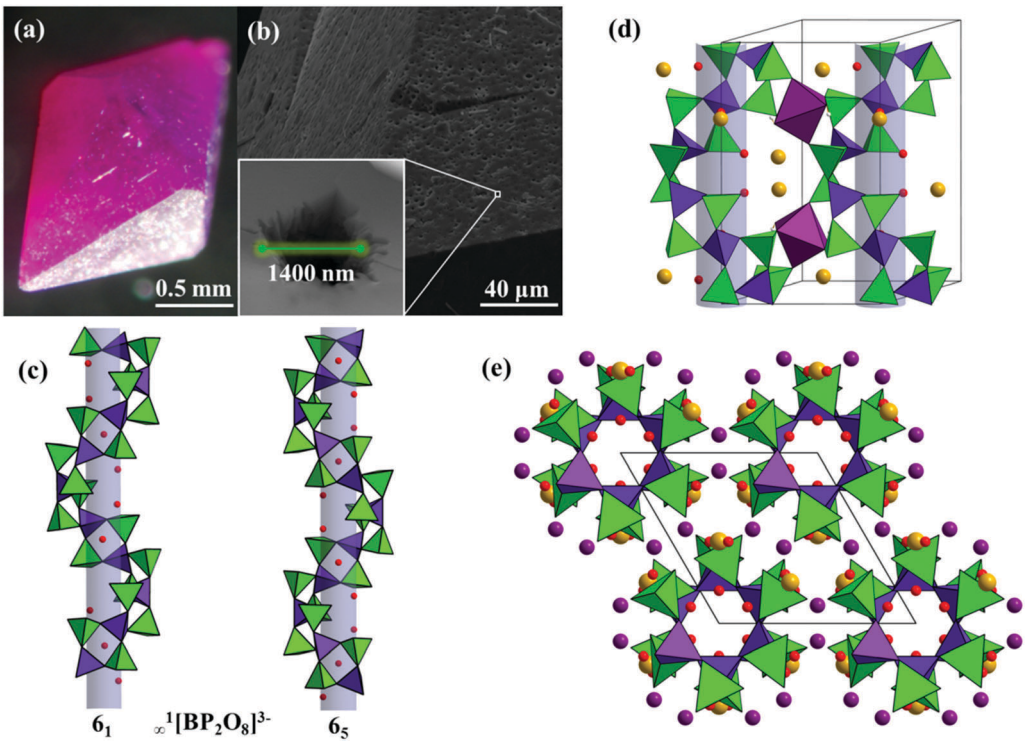

Fig. 1 Microscopic and structural aspects of helical borophosphates. (a) depicts the optical microscopic and (b), the SEM image of the porous single crystal of representative helical borophosphates (see Fig. S4–S6, ESI†). The crystals were deep pink in color and are porous hexagonal bipyramids in shape with a pore size of 1400 nm (inset (b) and Fig. S6, ESI†). (c) presents the anionic partial structure, $^1_\infty[BP_2O_8]^{3-}$, in the crystal structure of helical borophosphates built of four-membered rings of tetrahedra in which BO_4 (violet tetrahedra) and PO_4 (green tetrahedra) alternate and form a spiral ribbon of either a 6_1 or 6_5 helix. (d) Thus formed helices, $^1_\infty[BP_2O_8]^{3-}$, running along [001], are interconnected *via* $CoO_4(OH_2)_2$ (fuchsia) coordination octahedra (white spheres are protons) and the free threads of helices are occupied by M^I (yellow spheres; Li or Na) which are in an irregular surrounding of oxygen atoms. The hydrate water (red spheres) is located within the running helical channels. (e) illustrates the arrangement of the chains in a dense rod-packing motif along [001] (Co spheres are in fuchsia color).

with each other along the spiral and are located within the inner walls of helical channels (Fig. 1e) and play a key role in holding the structure together. Strikingly, this chiral architecture is closely related to the chiral zinc phosphate (CZP) topology.[45]

Electrocatalytic OER and HER performance

We first investigated the electrocatalytic OER performance of BPOs, electrophoretically deposited on fluorine doped tin oxide (FTO) in 1 M KOH (Fig. 2a). The overpotential for the OER was determined to be 293 mV at a current density of 10 mA cm^{-2} for **LiCoBPO** and 328 mV for **NaCoBPO** (Fig. S13, ESI†). Interestingly, the resulting overpotentials attained were some of the lowest compared to other cobalt-based materials as well as lower than most of the high-performance TM based catalysts (see Table S2, ESI†) reported so far on FTO (Table S4, ESI†).[46,47] While cycling, prior to the OER, a reversible redox couple was attained which could be attributed to Co^{2+}/Co^{3+}, and is typical for first-row TM based materials giving strong indication of the formation of the $M(OH)_2$/MOOH phase (Fig. 13a, ESI†).[48–50] The OER kinetics of BPOs was investigated using Tafel plots (Fig. S14, ESI†) where the Tafel slope of **LiCoBPO** (58 mV dec^{-1}) was superior to **NaCoBPO** (60 mV dec^{-1}). The Tafel slope is an inherent property of electrocatalytic materials which is indeed a valuable parameter of the rate-limiting step for reactions involving electron transfer. A Tafel slope close to 59 mV dec^{-1} (attained in our case) corresponds to the OER mechanism involving a reversible one-electron transfer prior to a chemical turnover-limiting step.[49,51–53] In order to gather more information on the intrinsic activity of the catalysts, the double-layer capacitances (C_{dl}) of the catalysts were determined. Fig S15c (ESI†) depicts the C_{dl} of the electrodes measured from the capacitive currents as a function of the scan rate obtained from the corresponding CV curves (Fig. S15a and b, ESI†).[47,54,55] The **LiCoBPO** exhibited highest C_{dl} (0.72 mF cm^{-2}) which was almost twice higher than **NaCoBPO** (0.42 mF cm^{-2}). As the electrocatalytic active surface area (ECSA) is generally considered to be a crucial parameter for increasing electrochemical activity, the C_{dl} were further converted into ECSA using the specific capacitance value for a standard with 1 cm^2 of exposed surface area (see Experimental).[47,54] The calculated active ECSA of **LiCoBPO** was 18 cm^2 whereas a value of 10.5 cm^2 was attained for **NaCoBPO**. The improved ECSA of **LiCoBPO** implies the greater exposure of active sites by favoring efficient adsorption and transfer of reactants.[9] Subsequently, electrochemical impedance spectroscopy (EIS) was performed to gain knowledge of the electron-transfer kinetics.[9] As shown in Fig. S15d (ESI†), the Nyquist plots obtained by EIS measurement indicated a small charge transfer resistance (R_{ct}) for **LiCoBPO** compared to **NaCoBPO**

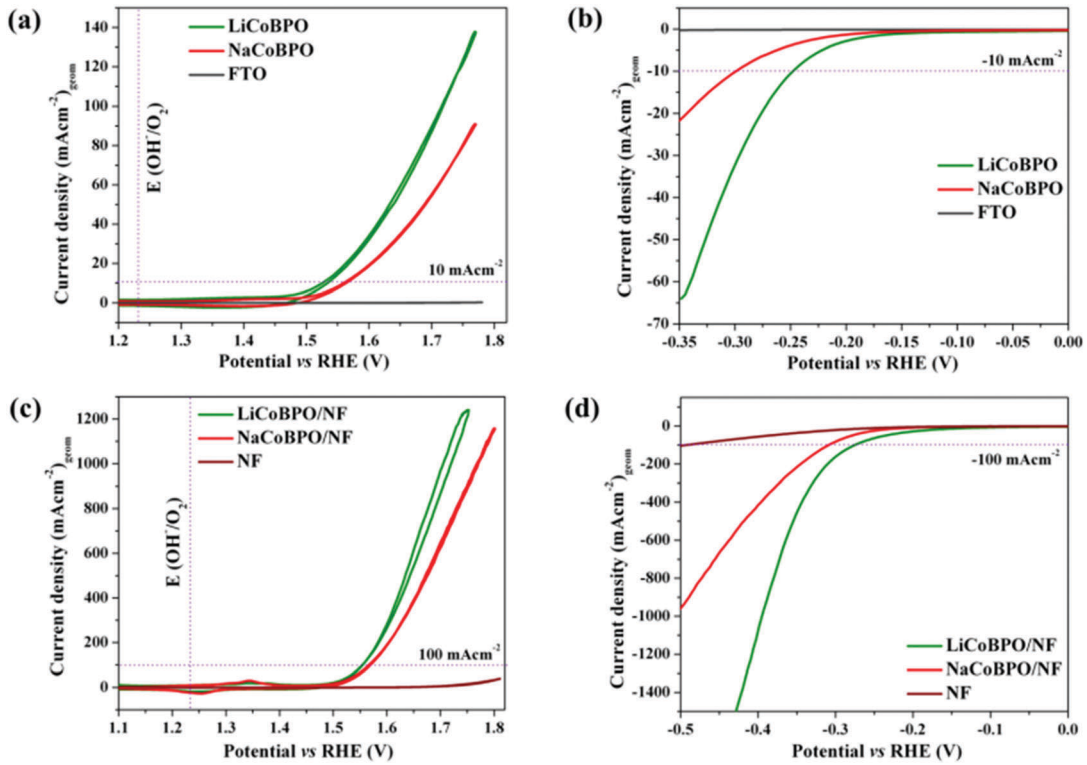

Fig. 2 Electrocatalytic performance of helical borophosphates (**LiCoBPO** and **NaCoBPO**) using a three-electrode system. (a) CV and (b) LSV on FTO, and (c) CV and (d) LSV on NF for the OER and HER in 1 M KOH electrolyte. The comparison with the state-of-the-art catalysts is presented in Fig. S17 and S40, ESI.†

signifying faster charge transport leading to higher catalytic activity. In addition to the presented BPOs, cobalt phosphate (Experimental; Fig. S16, ESI†) (430 mV) and state-of-the-art benchmarking catalysts RuO_2 (354 mV), IrO_2 (400 mV) and Pt were also electrophoretically deposited on FTO and measured for comparison at 10 mA cm^{-2}, and the catalytic activities of BPOs were excellent (Fig. S17a, ESI†). Separately, to have a direct correlation with Co-based catalysts, the catalytic OER activity of Co_3O_4 (360 mV), $Co(OH)_2$ (382 mV), CoOOH (401 mV) and metallic Co (430 mV) was also measured in similar conditions (Experimental; Fig. S18 and S19a, ESI†) that underlined the superiority of the BPOs as well as the need of a core–shell structure to enhance catalytic activity. The chronoamperometry (CA) of **LiCoBPO** and **NaCoBPO**, at OER conditions, at 1.53 and 1.56 V maintaining 10 mA cm^{-2}, produced constant current over 24 h (Fig. S20a, ESI†) for **LiCoBPO**.

The electrochemical HER performance of the catalysts was studied by linear sweep voltammetry (LSV) in 1 M KOH (Fig. 2b and Fig. 13b, ESI†). **LiCoBPO** proved to be a better catalyst with a 245 mV overpotential than **NaCoBPO** with 298 mV at −10 mA cm^{-2}. The resulting overpotential obtained for **LiCoBPO** is superior in comparison to the highly HER active oxides or phosphates and pretty much in the range of high-performance TM based catalysts on FTO (Table S3, ESI†).[46] The corresponding Tafel slope (Fig. S14, ESI†) of **LiCoBPO** was 98 mV dec^{-1}, which is lower than that of **NaCoBPO** (124 mV dec^{-1}). The obtained Tafel slope here suggests that the HER reaction on the BPO surface favors the Volmer–Heyrovsky mechanism where the water discharge (Volmer step) reaction is the rate-limiting step.[56,57] Additionally, the HER activity of BPOs was compared with noble metal catalysts Pt (42 mV) and IrO_2 (430 mV) as well as with the $Co_3(PO_4)_2{\cdot}8H_2O$ (358 mV), Co_3O_4 (n/a), $Co(OH)_2$ (n/a), CoOOH (n/a) and metallic Co (315 mV) catalysts at −10 mA cm^{-2} (Fig. S17–S19; ESI†). Except for Pt, the activity of other catalysts is significantly lower compared to BPOs. The CA responses of **LiCoBPO** and **NaCoBPO** for the HER were measured at −0.25 and −0.3 V upholding the current at almost −10 mA cm^{-2} for 24 h (Fig. 20b, ESI†).

Reversible switchable properties

Notably, the color of the working electrodes was completely transformed from pink to black during water oxidation and from pink to light brown during the HER indicating significant surface-structural changes. These color changes are switchable, *i.e.*, the black catalyst after the OER is transformed to light brown during the HER and *vice versa* under CV conditions. This illustrates that although the surface of the particles was transformed into active structures, the core of the particle still contained a substantial amount of **LiCoBPO** structure as indicated by the various experimental techniques (see GIXRD, TEM, XPS and *in situ* XAS results in the successive sections). The catalytic activities were also retained by the CA treatments (Fig. S21 and S22, ESI†). This type of switchable behavior of the catalysts has recently been reported for H_2-CoCat/O_2-CoCat (in phosphate buffer),[32] its Ni analog (in borate buffer)[34] and FeO_x (in KOH),[58]

but in all these catalysts associated with significantly lower catalytic activities and far less durability. In the case of **LiCoBPO**, the switchable property was achieved with excellent catalytic activities for both the OER and HER and the interconversion of these catalyst modifications was fully reversible.

Ex situ post catalytic characterization

The structural transformation and generation of the active sites during electrochemical operation were studied for **LiCoBPO**. Significant loss of Li from **LiCoBPO** was detected by ICP-AES measurements after operation at catalytic OER potentials suggesting lattice alterations leading to structural disorder with vacancies. However, the grazing incidence X-ray diffraction patterns (GIXRD) post OER and HER did not reveal any major structural differences when compared to the as-synthesized **LiCoBPO** (Fig. S23–S24; ESI†). Further, the FT-IR spectrum showed a sharp increase in the bands at 3320 cm^{-1} after OER CA confirming substantial hydroxylation (Fig. S25, ESI†). The presence of Co and P was also identified from the EDX analysis (Fig. S26 and S27, ESI†). The TEM investigation of **LiCoBPO** after OER CV showed the formation of a thin amorphous shell ($\sim$2 nm) on the surface of the particles and the thickness of the shell was further increased after CA ($>$20 nm), indicating the formation of the hydroxylated phase as discussed for other TM based catalysts in the literature (Fig. S28, ESI†).[48,49] However, this type of amorphous shell formation was not detected after HER LSV or CA, apart from the usual surface passivation to CoO (Fig. S29, ESI†).

The formation of the Co hydroxide-oxohydroxide species on the surface of the catalyst during OER was additionally proved by the Co 2p XPS spectra (Fig. S30, ESI†). Co(II) and Co(III) ions have almost similar 2p binding energies (BE) but can be distinguished by the Co $2p_{1/2}$–$2p_{3/2}$ spin–orbit level energy spacing, which is 16 eV for high-spin Co(II) and 15 eV for low-spin Co(III).[59] The Co $2p_{1/2}$–$2p_{3/2}$ spin–orbit spacing of 16 eV in the deposited catalyst was decreased to 15.6 eV after CV and 15.1 eV after CA. This result indicates that surface Co(II) species were oxidized to mixed Co(II,III) after CV and further oxidized during CA.[59] In the case of HER LSV and CA, the resultant spin–orbit spacing was 16.0 and 15.8 eV, indicating that there was not much change in the oxidation state during HER LSV but slight surface passivation during HER CA (Fig. S30, ESI†). The detailed deconvolution profiles and the resulting Co(II)/Co(III) ratio of the area of the Co 2p region are given in Fig. S31 and S32, and Tables S5 and S6 (ESI†). In the Li 1s region, both OER CV and HER LSV showed a peak at a BE of 55.5 eV but the surface composition revealed a significant loss of Li from the surface ($\sim$30%), and after CA, no Li was present on the surface designating total surface-structural rearrangements (Fig. S33).[60] The XPS studies of P 2p and B 1s after the electrochemical HER and OER did not reveal any detectable change in the coordination environments of phosphate (PO_4^{3-}) and borate (Fig. S34 and S35, ESI†).[61,62] The O 1s spectra clearly show the formation of surface hydroxide species, especially after the electrochemical OER treatment while the peak between 529 and 530 eV indicates the formation of oxidic species (CoO_x) on the surface (Fig. S36, ESI†).[48,63] The surface composition acquired in XPS is also consistent with the results of ICP-AES and EDX. Four probe resistivity measurements were additionally carried out on the FTO substrates which confirmed significantly higher charge mobility for the post OER and HER treated materials compared to the as-synthesized **LiCoBPO** (Table S7, ESI†).

Note that a substantially lower amount of Na was expelled from the structure of **NaCoBPO** under OER conditions (ICP-AES) in comparison to Li (due to higher coordination modes of Na in the structure), which explains the superior activity of **LiCoBPO** over **NaCoBPO**. Apart from this, a structural transformation similar to that of **LiCoBPO** is likely expected to occur for the Na-analogue.

In situ XAS characterization

To shed light on the local atomic and electronic structure, extended X-ray absorption fine-structure (EXAFS) and near-edge structure (XANES) studies were carried out under quasi *in situ* conditions (Fig. 3 and 4). After applying oxidizing potentials (Fig. 3a), the structure transforms to the one of the CoO_x catalyst (also known as CoCat).[64] On the contrary, in Fig. 3b, there is a clear metallic contribution visible in the spectrum of the catalyst after CA at reducing potentials (HER). After deposition of the **LiCoBPO** powder on the electrode, a slight shift of the edge energy position towards lower energy was seen; this could correspond to a slight decrease of the Co oxidation state (see Table S8, ESI†). The oxidation state of Co clearly increases after exposure to oxidizing potentials (Fig. 3 and Table S8, ESI†). The estimation of the Co oxidation state based on the edge energy position is difficult when there is a metallic phase present. That is why instead we used the bond valence sum, determined from the EXAFS simulation of the Co edge EXAFS spectra (see Fig. 4 and Tables S8–S14, ESI†).[64,65] The simulation shows that the **LiCoBPO** powder material corresponds well to the crystal structure (both with respect to coordination numbers and interatomic distances). After deposition on the electrode, there is a slight modification in the distances and coordination, but within the accuracy of the simulation parameters (Table S11, ESI†). The spectra of materials exposed to oxidizing potentials (OER) were simulated as a linear combination between the spectrum of the as-deposited material and the Co catalyst.[66] For both spectra (after CV and CA) similar results were obtained indicating that after exposure to an oxidizing potential part of the material is converted to the CoO_x structure. The CoO_x is more ordered than the typical Co catalyst as seen from the resolvable 'double' Co–Co distance, which is not visible in the electrodeposited oxides. However, even long exposure to an oxidizing potential does not result in a full conversion of the material. The spectra of the materials exposed to reducing potentials (HER LSV and HER CA) were simulated as a linear combination of three spectra: (i) the simulated spectrum of metallic Co, (ii) the spectrum of the as-deposited material, and (iii) the CoO(H) phase (Table S9, ESI†). In the material after LSV, there is the formation of CoO(H) and no detectable metallic contribution. After CA, the metallic contribution increases to about 40% and the CoO amount does not change significantly.

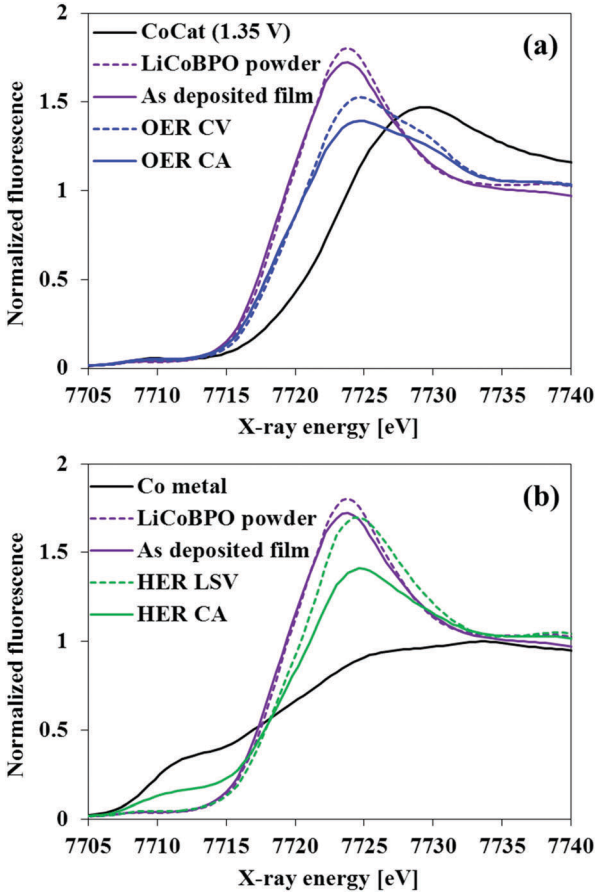

Fig. 3 *In situ* XANES spectra collected at the Co K edge. XANES spectra were measured for the as-prepared powder and as-deposited films of **LiCoBPO** and were compared with the (a) oxidizing (OER CV and OER CA) and (b) reducing (HER LSV and HER CA) environments. The metallic Co in (b) and CoCat in (a) were conditioned at 1.35 V (ref. 64) and used as references.

Insights into the active catalytic structure

The above results indicate that the helical BPOs act as pre-catalysts for water-splitting that are transformed to the catalytically active structures under electrochemical conditions. The fascinating structure of borophosphates provides the required flexibility in the structural transformation and simultaneously facilitates efficient electron transport within the network. A large number of water molecules inside the helical channels and coordinated to cobalt octahedra assist the proton-coupled electron transfer similar to extensive hydrogen bonding in a water network around the oxygen-evolving Mn_4CaO_5 cluster of photosystem II.[67] Interestingly, recent studies have also elucidated that solvation structures can greatly enhance the electron transfer rates.[68] Apart from the structural aspects, the superior O_2 evolution at anodic bias is attributed to (i) surface reorganization leading to lattice vacancies and defects due to the loss of Li or Na, (ii) the presence of a large amount of structural hydroxides that helps to form Co-oxyhydroxide/-hydroxides at the surface, which is considered to be a prerequisite for active-site formation in OER catalysis, (iii) the pronounced increase in the oxidation state of Co(II) to the higher oxidation state of Co by generation of an amorphous shell consisting of $Co(OH)_2$/CoOOH species and CoO_x (CoCat) at the particle surface, (iv) crystal water within the channels in the core of BPO that can further enhance the diffusion of ions and electrolytes exposing more active sites, and (v) a large electrochemically active surface area leading to more catalytically active reaction sites in the material and the faster charge transfer process at the electrode. Thus, the active species on the catalyst surface facilitate the adsorption of OH^- ions and accelerate the transport of electrons for the recombination of two oxygen atoms to give efficient O_2 evolution. On the other hand, metallic Co coated with CoO and **LiCoBPO** has a strong affinity for H-adsorption thus promoting formation of active sites and thereby explaining the high HER efficiency.[32]

Activities on a conductive foam substrate

Encouraged by the robust performance of BPOs for the HER and OER on FTO supports, we further set out to explore their electrochemical performance on nickel foam (NF) which has a large working surface area with low ion transport resistance and effective gas diffusion (Fig. 2c and d).[69–71] An impressive improvement in the catalytic OER performance was achieved where only 216 mV and 242 mV overpotentials are required to reach the current density of 10 mA cm^{-2} for **LiCoBPO** and **NaCoBPO**, respectively (Fig. S37a, ESI†). A smaller Tafel slope (Fig. S38a, ESI†) of **LiCoBPO** (62 mV dec^{-1}) indicated more favorable reaction kinetics than **NaCoBPO** (99 mV dec^{-1}). The C_{dl} of **LiCoBPO** (2.14 mF cm^{-2}) was twice as large as that of **NaCoBPO** (1.07 mF cm^{-2}) (Fig. S39, ESI†) and the calculated ECSA from C_{dl} was 1.25 cm^2 for **LiCoBPO** and 0.62 cm^2 for **NaCoBPO**, suggesting more active sites of **LiCoBPO** are accessible which is due to the structural reorganization owing to faster release of Li than Na (as determined by ICP-AES).[72–74] Further, the EIS measurement revealed that the charge transfer resistance R_{ct} of **LiCoBPO** was slightly lower compared to **NaCoBPO** implying a rapid charge transfer process (Fig. S39d, ESI†).[9] Similarly, for the HER, the overpotential acquired at −10 mA cm^{-2} was 121 mV for **LiCoBPO** and 207 mV for its sodium analog (Fig. 37b, ESI†). Besides, **LiCoBPO** displayed a Tafel slope of 121 mV dec^{-1} which was smaller compared to **NaCoBPO** (128 mV dec^{-1}) (Fig. S38b, ESI†). The overpotential of **LiCoBPO** in the OER (even at high catalytic currents of 10, 100 and 1000 mA cm^{-2}) was extremely low in comparison to the commercial noble metal-based catalysts or any established TM based catalyst system in alkaline media (Fig. S40, Tables S2, and S4, ESI†).[46,75–77] The achieved catalytic HER activities are also some of the best in comparison to the recently known oxides, chalcogenides or pnictides but lesser than mono-functional NiFe-, NiMo- or CoMo-alloys (Table S3; ESI†).[46] This superiority was further evidenced by measuring the active Co-based Co_3O_4, $Co(OH)_2$, CoOOH and metallic Co catalysts (see Fig. S41 for OER and HER overpotentials; ESI†). The CA measurements for the OER and HER established the excellent stability of the systems over 40 h (Fig. S42, ESI†). The closer view of the SEM images of the as-prepared and after OER CA materials further demonstrated the dramatic changes on the surface of the **LiCoBPO** crystallites (Fig. S43 and S44, ESI†) which influence the performance of the catalytic activity.

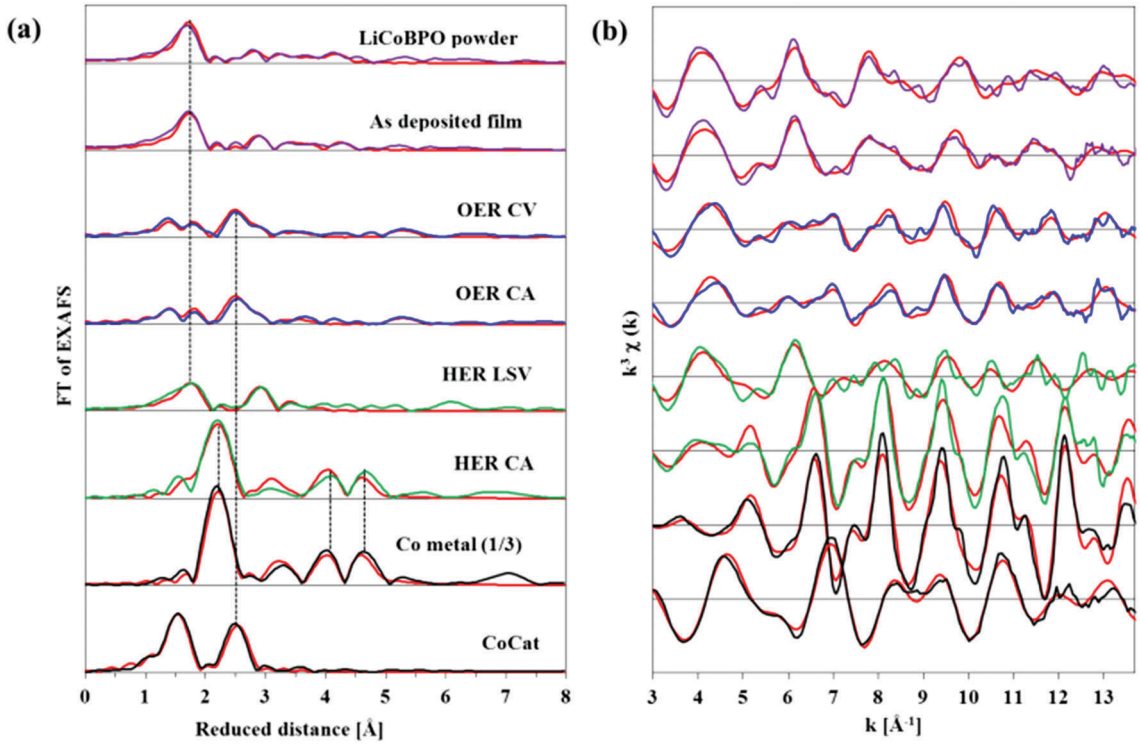

Fig. 4 *In situ* EXAFS spectra collected at the Co K edge. (a) presents the Fourier transform of the EXAFS spectra and (b) depicts the original k^3-weighted EXAFS spectra. For Fourier transformation a cosine window function, covering between 10% from the beginning and the end of the EXAFS range (3–14 $Å^{-1}$) was used. The experimental spectra are shown in magenta (non-treated compound), blue (after exposure to oxidizing potentials), green (after exposure to reducing potentials) and in black (the reference metallic Co and the Co oxide catalyst were taken from ref. 64). The simulated spectra are shown in red. The simulation parameters are given in Tables S9–S14 (ESI†). Vertical dotted lines indicate common structural motifs (interatomic distances) to guide the eye. For visibility, the amplitude of the spectrum of the metallic Co is reduced by a factor of 3.

Alkaline water-splitting device

The aforementioned outstanding OER and HER catalytic performance on NF verified the bifunctionality of these electrocatalyst materials and applicability as an anodic and cathodic catalyst for overall water-splitting. As envisioned, employment of the BPOs on both electrodes indeed facilitated excellent performance of overall water-splitting in a two-electrode configuration (**LiCoBPO**‖**LiCoBPO** and **NaCoBPO**‖**NaCoBPO**) (Fig. 5a and Fig. S45, ESI†). A cell voltage of only 1.53 V was achieved at 10 mA cm^{-2} for **LiCoBPO** whereas 1.58 V was attained for **NaCoBPO**, which are among the best values of current bifunctional electrocatalysts.[9,78,79] Based on the minimal electrical potential difference to split water (close to 1.23 V, related to Gibbs energies), these overall potentials correspond to energetic efficiencies exceeding the 75% level (78% for **NaCoBPO**, and 80% for **LiCoBPO**). Based on a higher heating value of H_2 gas, which here is assumed to correspond to an electrical potential difference of 1.48 V, the energetic efficiencies exceed the 90% level (94% for **NaCoBPO**, and 97% for **LiCoBPO**). Furthermore, the superior performance of BPOs for water electrolysis was compared to that of noble metal-based catalysts and is shown in Fig. S46 (ESI†).

For technological applications, long-term stability is required. Insufficient catalyst robustness indeed is a prominent problem and it is especially critical for catalyst materials based on non-noble metals.[80–82] In reports of new catalyst materials, stability often has not been assessed for time periods of technological relevance. Here, the durability of the electrodes was assessed at a potential supporting a current density of 10 mA cm^{-2}. The initial stable current over 90 h (inset, Fig. 5a) prompted us to explore **LiCoBPO** for a longer-stability run. An unceasing stability of two-and-a-half months was acquired with continuous growth in the current (Fig. 5b) demonstrating the undying nature of the catalysts which indeed renders the BPOs as highly promising catalysts for implementation in an integrated low-cost electrolyzer. The ICP-AES analysis of the electrodes post electrolysis confirmed no additional iron contamination apart from the NF (Fig. S47, ESI†) and therefore, we hypothesize that the increase in current density over time results from the Co-enriched surface-active sites with severe structural modifications (see Note 1; ESI†) rather than the incorporation of iron from KOH (Table S15, ESI†). The possible contribution of nickel (from the NF) was also ruled out by performing a controlled water-splitting experiment on bare NF at a potential of 1.53 V (cell potential of **LiCoBPO** at 10 mA cm^{-2}) as well as at 1.84 (cell potential of NF at 10 mA cm^{-2}) where only a decrease in the current density was attained (Fig. S48, ESI†). Moreover, the ICP-AES of the electrolyte after long-term measurements was measured, which disclosed negligible Ni leaching by further eliminating the possible incorporation of nickel in the structure or possible formation of $Ni(OH)_2$. In addition, a faradaic efficiency of ~100% for the HER and ~96% for the OER was obtained

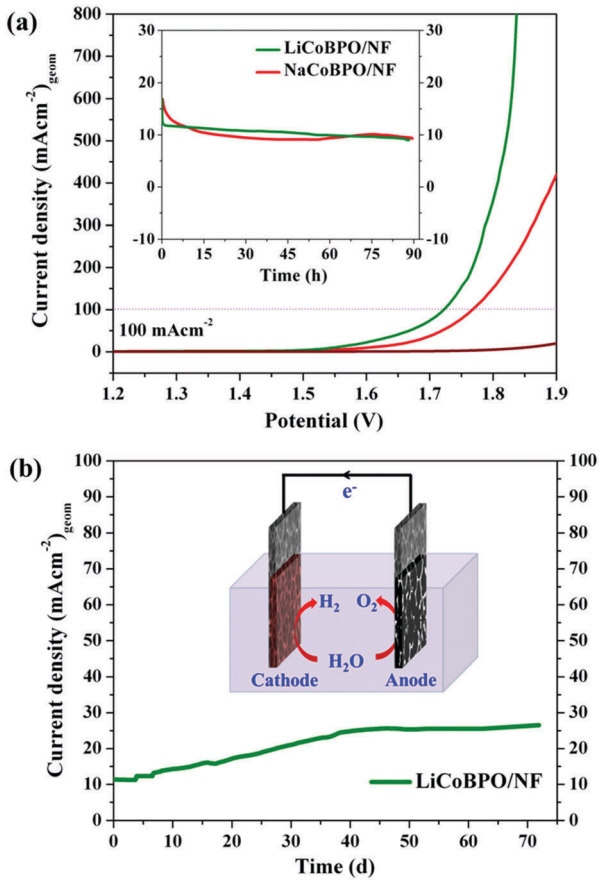

Fig. 5 Alkaline electrolyzer using the two electrode configuration. (a) is the current–potential plot of an alkaline electrolyzer using **LiCoBPO**‖**LiCoBPO** and **NaCoBPO**‖**NaCoBPO** on NF as both the cathode and anode (bare NF is shown in brown) in 1 M KOH with a scan rate of 5 mV s^{-1}. The comparison with the noble-metal system is shown in Fig. S46 (ESI†). The inset of (a) shows the stability of electrodes at an applied bias of 1.53 (**LiCoBPO**) and 1.58 V (**NaCoBPO**) (CA). The CA of **LiCoBPO** was further (b) investigated for ~73 days and yielded continuous growth in current demonstrating the undying nature of the catalysts. The inset of (b) shows the schematic view of an electrolyzer.

(Table S16, ESI†). An inverted electrochemical cell (graduated) was assembled to collect the evolved H_2 and O_2 at atmospheric pressure and the volumes and their ratios (~2 : 1) evolved were measured (Fig. S49 and S50, ESI†). Finally, a controlled two-electrode experiment of **LiCoBPO** was also performed on the FTO substrate that exhibited a cell potential of 1.94 V at a current density of 10 mA cm^{-2}. Strikingly, the long-term stability (at 1.95 V) test over 10 days also displayed continuous growth in current density over time demonstrating the fast and easy separation of Li and transformation of the material into a Co-rich surface as well as excluding the effect of the electrode substrate (Fig. S51, ESI†).

Conclusions

We have shown that helical metal borophosphates are not only aesthetically highly appealing materials. They also represent a new class of catalyst precursor material which is transformed under operation conditions into either OER or HER catalysts, both with excellent characteristics regarding energetic efficiency and long-term stability. The possibilities of tuning catalyst properties have been demonstrated by comparison of lithium and sodium as redox-inert metal ions in the helical borophosphate; further catalyst optimization could result from the exchange of cobalt ions against other redox-active metals. We consider that this material class may also provide new opportunities in other electrocatalytic applications, *e.g.* the reverse processes of oxygen reduction and hydrogen uptake reactions or the dark photosynthesis of fuels.

Experimental

Synthesis of $LiCo(H_2O)_2[BP_2O_8]\cdot H_2O$ (LiCoBPO)

Single crystals of $LiCo(H_2O)_2[BP_2O_8]\cdot H_2O$ were prepared by mild hydrothermal synthesis. For $LiCo(H_2O)_2[BP_2O_8]\cdot H_2O$, a mixture of 2.002 g of $Co(CH_3COO)_2\cdot 4H_2O$, and 2.715 g $Li_2B_4O_7$ was placed in 20 mL of distilled water. Subsequently, 5.554 g of H_3PO_4 (85%) was added to the mixture and the pH was adjusted to 1 by addition of 2 mL HCl (37%). The mixture was then transferred into a 50 mL Teflon-lined autoclave (filling degree ~30%), treated under autogenous pressure at 180 °C for three days, and cooled down naturally to ambient temperature. The reaction product was separated by centrifugation, washed with distilled water and acetone several times and dried overnight in air at 60 °C. The product consisted of pink hexagonal bipyramid crystals with dimensions ranging from 0.1 mm to 0.5 mm.

Synthesis of $NaCo(H_2O)_2[BP_2O_8]\cdot H_2O$ (NaCoBPO)

For $NaCo(H_2O)_2[BP_2O_8]\cdot H_2O$, a mixture of 2.005 g of $Co(CH_3COO)_2\cdot 4H_2O$, and 3.221 g $Na_2B_4O_7$ was placed in 20 mL of distilled water. Subsequently, 5.554 g of H_3PO_4 (85%) was added to the mixture and the pH was adjusted to 1 by addition of 2 mL HCl (37%). The further experimental procedure was continued as used for $LiCo(H_2O)_2[BP_2O_8]\cdot H_2O$. The separated pink crystals were washed thoroughly and dried overnight in air at 60 °C. The dimensions of the crystals obtained here were also in a similar range as observed for $LiCo(H_2O)_2[BP_2O_8]\cdot H_2O$.

Synthesis of $Co_3(PO_4)_2\cdot 8H_2O$

In a typical synthesis, 0.5 g of $Na_3PO_4\cdot 12H_2O$ was first dissolved in 20 mL of H_2O. To this solution, a second solution, which was formed by previously dissolving 0.5 g of $Co(CH_3COO)_2\cdot 4H_2O$ in 10 mL H_2O, was added dropwise. Immediate violet precipitation was observed, and the solution was further stirred for 3 hours. The final product was separated by centrifugation, washed with distilled water and ethanol several times and dried overnight in air.

Synthesis of CoOOH

Commercially available $Co(OH)_2$ was dispersed in 30 mL 4 M KOH solution which was then heated slowly up to 45 °C. 2 mL of 30% H_2O_2 solution was then added dropwise and was kept at the same temperature for 18 h. The final brown precipitate was

filtered and washed with deionized water three times, then dried at 65 °C overnight in air.

Instrument details

X-ray diffraction. Identification of the sample phases was determined using PXRD on a Bruker AXS D8 advanced automatic diffractometer equipped with a position sensitive detector (PSD) and a curved germanium (111) primary monochromator. Cu-Kα (λ = 1.5418 Å) radiation was used and the XRD profiles recorded were in the range of $5^\circ < 2\theta < 80^\circ$. The diffraction pattern fitting was conducted using the program WinxPow. The Rietveld analysis was carried out using the program FullProof where a theoretical line profile is calculated from a structural model that is refined using a least-squares approach until it matches the discrete data. The identified final structural models were drawn with the DIAMOND program version 3.0. GIXRD was recorded in the Bragg–Brentano geometry, using a Bruker AXS (D8 Advance) diffractometer with Cu-Kα radiation.

Elemental analysis. The chemical composition of the as-synthesized lithium or sodium cobalt borophosphates, as well as the dissolution of metal ions in the electrolyte during electrochemical conditions, was confirmed by ICP-AES on a Thermo Jarrell Ash Trace Scan analyzer. The as-synthesized materials were dissolved in acid solutions (aqua regia) whereas the electrolytes after the electrochemistry were taken directly for analysis. The results of three independent measurements were averaged. The composition of the as-synthesized materials showed good agreement with the chemical formulae.

Electron microscopy. SEM was carried out to examine texture, morphology and surface details of the crystals under investigation whereas EDX analyses were used to semi-quantitatively evaluate the presence of cobalt and phosphorous present on the sample surfaces. The elements with lower atomic numbers such as lithium and boron were not determined due to the detection limits. The samples were placed on a silicon wafer and the measurements were carried out on an LEO DSM 982 microscope integrated with EDX (EDAX, Appollo XPP). Data handling and analysis were conducted with the software package EDAX. The SEM images of the material on nickel foam electrode were taken on a Helios NanoLab G3 UC DualBeam (FIB/SEM system) from the company FEI operated at an accelerating voltage of 5 kV.

The microstructure investigations of the as-synthesized materials and the materials after electrochemical investigations were carried out using TEM analysis. A small amount of the powder was placed on a TEM-grid (carbon film on a 300 mesh Cu-grid, Plano GmbH, Wetzlar, Germany). The microstructure (particle size, morphology, crystallinity, and phase composition) of the materials was studied using an FEI Tecnai G^2 20 S-TWIN transmission electron microscope (FEI Company, Eindhoven, Netherlands) equipped with a LaB_6-source at a 200 kV acceleration voltage. The EDX analysis was performed with an EDAX r-TEM SUTW detector (Si (Li)-detector). Images were recorded with a GATAN MS794 P CCD-camera. Both SEM and TEM experiments were carried out at the Zentrum für Elektronenmikroskopie (ZELMI) of the TU Berlin.

Thermal analysis. In order to understand the information on decompositions, phase transitions and recrystallization events, simultaneous constant rate TGA and DTG analyses of the well ground as-synthesized materials were performed on a Rubotherm setup. The materials were first dried at 80 °C and were then placed in an open alumina crucible and heated at 5 K min^{-1} to 800 °C in a continuous nitrogen gas flow and cooled down to room temperature. The TG curves were corrected by subtraction of a blank run.

FT-IR spectroscopy. The presence of different modes of vibrations of the as-synthesized materials was studied using a BIORAD FTS 6000 FTIR spectrometer under attenuated total reflection (ATR) conditions. The data were recorded in the range of 400–4000 cm^{-1} with an average of 32 scans at 4 cm^{-1} resolution. Further, the presence of –OH groups and H_2O in the crystal structures of the investigated borophosphates was directly compared with the literature known examples.[41]

Brunauer–Emmett–Teller (BET) surface area. The surface areas and the pore size distributions of the materials were determined on a Quantachrome Autosorb1 apparatus. Nitrogen adsorption/desorption isotherms were measured at −196 °C after degassing the sample at 120 °C overnight. The BET surface areas (S_{BET}) were calculated from the adsorption data in a relative pressure ranging from 0.01 to 0.1.

Four-point probe resistivity measurements. The resistivity was measured using a Signature Pro4 system with a Keithley 2400 source-measure unit (SP4-40045TBY) using a four-point probe resistivity technique. The spacing between tungsten carbide tips was 1.016 mm with a radius of 0.245 mm and the spring pressure was 45 grams. The borophosphates were electrophoretically deposited on FTO to estimate the specific resistivity of each synthesized material and the average results are presented.

XPS measurements. The XPS measurements were conducted using a Kratos Axis Ultra X-ray photoelectron spectrometer (Kratos Analytical Ltd, Manchester, UK) with an Al Kα (1486.7 eV) monochromatic radiation source with a 90° takeoff angle (normal to the analyzer). The vacuum pressure in the analyzing chamber was kept at 2×10^{-9} Torr. The high-resolution XPS spectra were collected for C 1s, O 1s and Co 2p levels with pass energy 20 eV and step size 0.1 eV. The binding energies were then calibrated relative to the C 1s peak energy position at 285.0 eV. Analyses of the data were carried out using Casa XPS (Casa Software Ltd) and Vision data processing programs (Kratos Analytical Ltd).

***In situ* X-ray absorption spectroscopy (XAS).** The *in situ* X-ray absorption spectra (XANES/EXAFS) were collected at the BESSY synchrotron radiation source operated by the Helmholtz-Zentrum Berlin.[83] The measurements were conducted at the KMC-3 bending-magnet beamline at 20 K in a helium-flow cryostat (Oxford-Danfysik). The incident beam energy was selected by a Si(111) double-crystal monochromator. The measurements at the cobalt K-edge were performed in transmission mode with an ionization chamber and in fluorescence mode using a 13-element energy-resolving Ge detector (Canberra). The extracted spectrum was weighted by k^3 and simulated in k-space (E_0 = 6547 eV). All EXAFS simulations were performed

using in-house software (SimX) after calculation of the phase functions with the FEFF program (version 8.4, self-consistent field option activated).[84,85] The data range used in the simulation of the EXAFS spectra was 20–1000 eV (3–16 $Å^{-1}$). The EXAFS simulation was optimized by a minimization of the error sum obtained by summation of the squared deviations between measured and simulated values (least-squares fit). The fit was performed using the Levenberg-Marquardt method with numerical derivatives. The error ranges of the fit parameters were estimated from the covariance matrix of the fit. Further details are given elsewhere.[65,66,83]

LiCoBPO samples for XAS experiments were prepared on fluorinated tin oxide substrates in analogy to the electrochemical experiments. The samples were electrochemically treated for OER CV (3 cycles), HER LSV (3 cycles) and OER CA (25 h) at 1.53 V *vs.* RHE and HER CA (25 h) at −0.25 V *vs.* RHE (maintaining a current density of 10 and −10 mA cm^{-2}) for 24 hours in 1 M KOH solutions. After the desired electrochemical measurement, the samples were immediately freeze-quenched using liquid N_2 under vigorous N_2 gas flow and stored in liquid N_2 until XAS measurements were conducted.

Gas chromatography. An Agilent 7890A gas chromatograph (GC) was used to determine the hydrogen and oxygen contents in the headspace. The GC was equipped with a carboxen-1000 column and a thermal conductivity detector (TCD). The carrier gas was argon (Ar). The catalysts were first immersed in the 53 mL closed electrolyzer set-up and bubbled with Ar for 1 h. Subsequently, the gas in the headspace was taken with a syringe and injected into the GC. After the experiment, the amount of H_2 and O_2 collected in the head-space was determined. The aerial O_2 contribution during sampling was corrected by estimating O_2 before and after the electrochemical reaction.

Electrochemical measurements

First of all, the single crystals of **LiCoBPO** and **NaCoBPO** were placed in a mortar and thoroughly ground for 5 minutes using a pestle (S_{BET} is 1.30 m^2 g^{-1} and 2.45 m^2 g^{-1}). The electrodes used for electrochemical measurements were prepared by electrophoretic deposition (EPD) with a potential difference of 10 V in a mixture of a minimum amount of iodine (for 50 mg of catalyst, 3 mg of iodine) and acetone on a 1 × 1 cm^2 area of fluorinated tin oxide coated glass (FTO, Sigma Aldrich, resistivity 8–12 Ω $sq.^{-1}$). The EPD was carried out for 3 minutes for each FTO electrode. The loading of the deposited materials on each electrode was weighed and the amount obtained was ∼1 mg cm^{-2}. The catalytic activity of the materials was then measured in 1 M KOH solution at room temperature using a single-compartment three-electrode electrochemical cell (material deposited on FTO-glass as a working electrode, Pt wire as a counter electrode and Hg/Hg_2SO_4 (CH instruments) as a reference electrode) with a potentiostat (SP-200, BioLogic Science Instruments) controlled by the EC-Lab v10.20 software package.

Cyclic voltammetry (CV) and linear sweep voltammetry (LSV) were conducted with the typical electrolyte resistance and an *iR* compensation of 80% was applied. The electrolyte was not stirred during the electrochemical experiments. The potentials reported in the presented work were referenced to the reversible hydrogen electrode (RHE) through RHE calibration, and in 1 M KOH at pH 14, $E(RHE) = E(Hg/Hg_2SO_4) + 0.64 + (0.0591 \times pH)$ V. The Tafel slopes were derived from OER and HER polarization curves obtained at 1 mV s^{-1}. The active ECSA was assessed from the electrochemical double-layer capacitance (C_{dl}) of the catalytic surface and the electrochemical capacitance was obtained by measuring the non-faradaic capacitive current related to double-layer charging from the scan-rate dependence of CVs. The C_{dl} values of the materials were converted into ECSA according to the equation ECSA = C_{dl}/C_s where C_s is the specific capacitance of the material for a standard with 1 cm^2 of real surface area under identical electrolyte conditions. For measuring the ECSA, the general specific capacitances C_s = 0.040 mF cm^2 for FTO and C_s = 1.7 mF cm^2 for NF in 1 M KOH electrolyte were used based on typical reported values.[47,54,74] To evaluate the electron transfer resistance at the catalyst/electrolyte interface, EIS was conducted. EIS was performed at 1.5 V (*vs.* RHE). A sinusoidal voltage with an amplitude of 5 mV and scanning frequency ranging from 100 kHz to 1 Hz was applied to carry out the measurements. The impedance spectra were fitted using a simplified Randles equivalent circuit. The chronoamperometric measurements were performed in 1 M KOH at selected constant potentials (at a current density of 10 mA cm^{-2}) *vs.* RHE to reveal the long-term stability of the materials.

In addition to the FTO, the deposition of the materials on nickel foam (NF, Racemat BV) electrodes was also realized by EPD and the obtained loading of the material on the NF electrode was ∼3 mg cm^{-2}. CV, LSV, ECSA, EIS, and long-term chronoamperometric measurements were also performed on NF similarly to the FTO electrodes. The overall water-splitting reaction was performed in a two-electrode system on materials deposited on NF or FTO and subsequently, the long-term durability was also tested at a selected potential, when the current reached 10 mA cm^{-2}.

Conflicts of interest

There are no conflicts to declare.

Acknowledgements

Financial support by the Deutsche Forschungsgemeinschaft (Cluster of Excellence UniCat, EXC 314-2) is gratefully acknowledged. The authors are indebted to Dr Vitaly Gutkin for XPS, Dr Marc Willinger and Mr Christoph Fahrenson for SEM measurements.

Notes and references

1 A. S. Arico, P. Bruce, B. Scrosati, J. M. Tarascon and W. van Schalkwijk, *Nat. Mater.*, 2005, **4**, 366–377.
2 L. Hammarstrom, J. R. Winkler, H. B. Gray and S. Styring, *Science*, 2011, **333**, 288.
3 H. B. Gray, *Nat. Chem.*, 2009, **1**, 7.

4 H. Dau, E. Fujita and L. C. Sun, *ChemSusChem*, 2017, **10**, 4228–4235.
5 T. J. Meyer, *Nature*, 2008, **451**, 778–779.
6 M. G. Walter, E. L. Warren, J. R. McKone, S. W. Boettcher, Q. X. Mi, E. A. Santori and N. S. Lewis, *Chem. Rev.*, 2010, **110**, 6446–6473.
7 P. W. Menezes, C. Panda, S. Loos, F. Bunschei-Bruns, C. Walter, M. Schwarze, X. Deng, H. Dau and M. Driess, *Energy Environ. Sci.*, 2018, **11**, 1287–1298.
8 E. L. Hu, Y. F. Feng, J. W. Nai, D. Zhao, Y. Hu and X. W. Lou, *Energy Environ. Sci.*, 2018, **11**, 872–880.
9 L. Yu, H. Q. Zhou, J. Y. Sun, F. Qin, F. Yu, J. M. Bao, Y. Yu, S. Chen and Z. F. Ren, *Energy Environ. Sci.*, 2017, **10**, 1820–1827.
10 Y. Jiao, Y. Zheng, M. T. Jaroniec and S. Z. Qiao, *Chem. Soc. Rev.*, 2015, **44**, 2060–2086.
11 S. Cherevko, S. Geiger, O. Kasian, N. Kulyk, J. P. Grote, A. Savan, B. R. Shrestha, S. Merzlikin, B. Breitbach, A. Ludwig and K. J. J. Mayrhofer, *Catal. Today*, 2016, **262**, 170–180.
12 N. T. Suen, S. F. Hung, Q. Quan, N. Zhang, Y. J. Xu and H. M. Chen, *Chem. Soc. Rev.*, 2017, **46**, 337–365.
13 P. C. K. Vesborg, B. Seger and I. Chorkendorff, *J. Phys. Chem. Lett.*, 2015, **6**, 951–957.
14 C. Wei, Z. X. Feng, G. G. Scherer, J. Barber, Y. Shao-Horn and Z. C. J. Xu, *Adv. Mater.*, 2017, **29**, 1606800.
15 I. Roger, M. A. Shipman and M. D. Symes, *Nat. Rev. Chem.*, 2017, **1**, 0003.
16 L. A. Stern, L. G. Feng, F. Song and X. L. Hu, *Energy Environ. Sci.*, 2015, **8**, 2347–2351.
17 Q. Zhao, Z. H. Yan, C. C. Chen and J. Chen, *Chem. Rev.*, 2017, **117**, 10121–10211.
18 M. M. Najafpour, G. Renger, M. Holynska, A. N. Moghaddam, E. M. Aro, R. Carpentier, H. Nishihara, J. J. Eaton-Rye, J. R. Shen and S. I. Allakhverdiev, *Chem. Rev.*, 2016, **116**, 2886–2936.
19 Y. P. Liu, X. Liang, L. Gu, Y. Zhang, G. D. Li, X. X. Zou and J. S. Chen, *Nat. Commun.*, 2018, **9**, 2609.
20 Y. C. Chen, A. Y. Lu, P. Lu, X. L. Yang, C. M. Jiang, M. Mariano, B. Kaehr, O. Lin, A. Taylor, I. D. Sharp, L. J. Li, S. S. Chou and V. Tung, *Adv. Mater.*, 2017, **29**, 1703863.
21 J. Z. Liu, Y. F. Ji, J. W. Nai, X. G. Niu, Y. Luo, L. Guo and S. H. Yang, *Energy Environ. Sci.*, 2018, **11**, 1736–1741.
22 H. Schafer, D. M. Chevrier, P. Zhang, J. Stangl, K. Muller-Buschbaum, J. D. Hardege, K. Kuepper, J. Wollschlager, U. Krupp, S. Duhnen, M. Steinhart, L. Walder, S. Sadaf and M. Schmidt, *Adv. Funct. Mater.*, 2016, **26**, 6402–6417.
23 M. W. Kanan and D. G. Nocera, *Science*, 2008, **321**, 1072–1075.
24 Y. B. Li and C. Zhao, *Chem. Mater.*, 2016, **28**, 5659–5666.
25 H. S. Ahn and T. D. Tilley, *Adv. Funct. Mater.*, 2013, **23**, 227–233.
26 H. Kim, J. Park, I. Park, K. Jin, S. E. Jerng, S. H. Kim, K. T. Nam and K. Kang, *Nat. Commun.*, 2015, **6**, 8253.
27 D. Gonzalez-Flores, I. Sanchez, I. Zaharieva, K. Klingan, J. Heidkamp, P. Chernev, P. W. Menezes, M. Driess, H. Dau and M. L. Montero, *Angew. Chem., Int. Ed.*, 2015, **54**, 2472–2476.
28 Y. Y. Liu, H. T. Wang, D. C. Lin, C. Liu, P. C. Hsu, W. Liu, W. Chen and Y. Cui, *Energy Environ. Sci.*, 2015, **8**, 1719–1724.
29 N. Jiang, B. You, M. L. Sheng and Y. J. Sun, *Angew. Chem., Int. Ed.*, 2015, **54**, 6251–6254.
30 Y. Yang, H. L. Fei, G. D. Ruan and J. M. Tour, *Adv. Mater.*, 2015, **27**, 3175–3180.
31 M. W. Kanan, Y. Surendranath and D. G. Nocera, *Chem. Soc. Rev.*, 2009, **38**, 109–114.
32 S. Cobo, J. Heidkamp, P. A. Jacques, J. Fize, V. Fourmond, L. Guetaz, B. Jousselme, V. Ivanova, H. Dau, S. Palacin, M. Fontecave and V. Artero, *Nat. Mater.*, 2012, **11**, 802–807.
33 A. J. Esswein, Y. Surendranath, S. Y. Reece and D. G. Nocera, *Energy Environ. Sci.*, 2011, **4**, 499–504.
34 C. Y. He, X. L. Wu and Z. Q. He, *J. Phys. Chem. C*, 2014, **118**, 4578–4584.
35 X. Q. Ji, L. Cui, D. N. Liu, S. Hao, J. Q. Liu, F. L. Qu, Y. J. Ma, G. Du, A. M. Asiri and X. P. Sun, *Chem. Commun.*, 2017, **53**, 3070–3073.
36 P. Z. Chen, K. Xu, T. P. Zhou, Y. Tong, J. C. Wu, H. Cheng, X. L. Lu, H. Ding, C. Z. Wu and Y. Xie, *Angew. Chem., Int. Ed.*, 2016, **55**, 2488–2492.
37 B. Ewald, Y. X. Huang and R. Kniep, *Z. Anorg. Allg. Chem.*, 2007, **633**, 1517–1540.
38 G. Hautier, A. Jain, H. L. Chen, C. Moore, S. P. Ong and G. Ceder, *J. Mater. Chem.*, 2011, **21**, 17147–17153.
39 P. W. Menezes, S. Hoffmann, Y. Prots and R. Kniep, *Z. Kristallogr. – New Cryst. Struct.*, 2006, **221**, 251–252.
40 P. W. Menezes, PhD thesis, Technical University of Dresden, 2009.
41 P. W. Menezes, S. Hoffmann, Y. Prots and R. Kniep, *Z. Kristallogr. – New Cryst. Struct.*, 2008, **223**, 333–334.
42 Y. Tanaka, T. Takeuchi, S. W. Lovesey, K. S. Knight, A. Chainani, Y. Takata, M. Oura, Y. Senba, H. Ohashi and S. Shin, *Phys. Rev. Lett.*, 2008, **100**, 145502.
43 J. D. Watson and F. H. C. Crick, *Nature*, 1953, **171**, 737–738.
44 R. Kniep, H. G. Will, I. Boy and C. Rohr, *Angew. Chem., Int. Ed.*, 1997, **36**, 1013–1014.
45 W. T. A. Harrison, T. E. Gier, G. D. Stucky, R. W. Broach and R. A. Bedard, *Chem. Mater.*, 1996, **8**, 145–151.
46 C. C. L. McCrory, S. Jung, I. M. Ferrer, S. M. Chatman, J. C. Peters and T. F. Jaramillo, *J. Am. Chem. Soc.*, 2015, **137**, 4347–4357.
47 C. C. L. McCrory, S. H. Jung, J. C. Peters and T. F. Jaramillo, *J. Am. Chem. Soc.*, 2013, **135**, 16977–16987.
48 P. W. Menezes, A. Indra, A. Bergmann, P. Chernev, C. Walter, H. Dau, P. Strasser and M. Driess, *J. Mater. Chem. A*, 2016, **4**, 10014–10022.
49 M. S. Burke, M. G. Kast, L. Trotochaud, A. M. Smith and S. W. Boettcher, *J. Am. Chem. Soc.*, 2015, **137**, 3638–3648.
50 D. Friebel, M. W. Louie, M. Bajdich, K. E. Sanwald, Y. Cai, A. M. Wise, M. J. Cheng, D. Sokaras, T. C. Weng, R. Alonso-Mori, R. C. Davis, J. R. Bargar, J. K. Norskov, A. Nilsson and A. T. Bell, *J. Am. Chem. Soc.*, 2015, **137**, 1305–1313.
51 Y. Surendranath, M. W. Kanan and D. G. Nocera, *J. Am. Chem. Soc.*, 2010, **132**, 16501–16509.
52 J. Park, Y. J. Sa, H. Baik, T. Kwon, S. H. Joo and K. Lee, *ACS Nano*, 2017, **11**, 5500–5509.

53 T. Shinagawa, A. T. Garcia-Esparza and K. Takanabe, *Sci. Rep.*, 2015, **5**, 13801.
54 Q. Kang, L. Vernisse, R. C. Remsing, A. C. Thenuwara, S. L. Shumlas, I. G. McKendry, M. L. Klein, E. Borguet, M. J. Zdilla and D. R. Strongin, *J. Am. Chem. Soc.*, 2017, **139**, 1863–1870.
55 J. G. Hou, Y. Z. Wu, S. Y. Cao, Y. Q. Sun and L. C. Sun, *Small*, 2017, **13**, 1702018.
56 C. G. Morales-Guio, L. A. Stern and X. L. Hu, *Chem. Soc. Rev.*, 2014, **43**, 6555–6569.
57 H. Li, P. Wen, Q. Li, C. C. Dun, J. H. Xing, C. Lu, S. Adhikari, L. Jiang, D. L. Carroll and S. M. Geyer, *Adv. Energy Mater.*, 2017, **7**, 1700513.
58 B. C. M. Martindale and E. Reisner, *Adv. Energy Mater.*, 2016, **6**, 1502095.
59 D. C. Frost, C. A. McDowell and I. S. Woolsey, *Mol. Phys.*, 1974, **27**, 1473–1489.
60 A. W. Moses, H. G. G. Flores, J. G. Kim and M. A. Langell, *Appl. Surf. Sci.*, 2007, **253**, 4782–4791.
61 X. Y. Sun, Y. X. Ding, B. S. Zhang, R. Huang and D. S. Su, *Chem. Commun.*, 2015, **51**, 9145–9148.
62 Z. G. Zhao, J. Zhang, Y. Y. Yuan, H. Lv, Y. Y. Tian, D. Wu and Q. W. Li, *Sci. Rep.*, 2013, **3**, 2263.
63 A. Indra, P. W. Menezes, C. Das, C. Gobel, M. Tallarida, D. Schmeisser and M. Driess, *J. Mater. Chem. A*, 2017, **5**, 5171–5177.
64 M. Risch, F. Ringleb, M. Kohlhoff, P. Bogdanoff, P. Chernev, I. Zaharieva and H. Dau, *Energy Environ. Sci.*, 2015, **8**, 661–674.
65 I. Zaharieva, P. Chernev, M. Risch, K. Klingan, M. Kohlhoff, A. Fischer and H. Dau, *Energy Environ. Sci.*, 2012, **5**, 7081–7089.
66 M. Risch, V. Khare, I. Zaharieva, L. Gerencser, P. Chernev and H. Dau, *J. Am. Chem. Soc.*, 2009, **131**, 6936–6937.
67 Y. Umena, K. Kawakami, J. R. Shen and N. Kamiya, *Nature*, 2011, **473**, 55–U65.
68 R. C. Remsing, I. G. McKendry, D. R. Strongin, M. L. Kein and M. J. Zdilla, *J. Phys. Chem. Lett.*, 2015, **6**, 4804–4808.
69 X. Y. Lu and C. A. Zhao, *Nat. Commun.*, 2015, **6**, 6616.
70 H. Q. Zhou, F. Yu, Y. F. Huang, J. Y. Sun, Z. Zhu, R. J. Nielsen, R. He, J. M. Bao, W. A. Goddard, S. Chen and Z. F. Ren, *Nat. Commun.*, 2016, **7**, 12765.
71 X. G. Wang, Y. V. Kolen'ko, X. Q. Bao, K. Kovnir and L. F. Liu, *Angew. Chem., Int. Ed.*, 2015, **54**, 8188–8192.
72 B. You and Y. J. Sun, *Adv. Energy Mater.*, 2016, **6**, 1502333.
73 Y. Q. Yang, K. Zhang, H. L. Ling, X. Li, H. C. Chan, L. C. Yang and Q. S. Gao, *ACS Catal.*, 2017, **7**, 2357–2366.
74 H. F. Liang, A. N. Gandi, D. H. Anjum, X. B. Wang, U. Schwingenschlogl and H. N. Alshareef, *Nano Lett.*, 2016, **16**, 7718–7725.
75 B. M. Hunter, H. B. Gray and A. M. Muller, *Chem. Rev.*, 2016, **116**, 14120–14136.
76 P. Xiao, W. Chen and X. Wang, *Adv. Energy Mater.*, 2015, **5**, 1500985.
77 M. Gong, D. Y. Wang, C. C. Chen, B. J. Hwang and H. J. Dai, *Nano Res.*, 2016, **9**, 28–46.
78 Y. Yan, B. Y. Xia, B. Zhao and X. Wang, *J. Mater. Chem. A*, 2016, **4**, 17587–17603.
79 Y. Wang, B. Kong, D. Y. Zhao, H. T. Wang and C. Selomulya, *Nano Today*, 2017, **15**, 26–55.
80 J. R. McKone, N. S. Lewis and H. B. Gray, *Chem. Mater.*, 2014, **26**, 407–414.
81 S. Y. Tee, K. Y. Win, W. S. Teo, L. D. Koh, S. H. Liu, C. P. Teng and M. Y. Han, *Adv. Sci.*, 2017, **4**, 1600337.
82 W. Li, X. F. Gao, X. G. Wang, D. H. Xiong, P. P. Huang, W. G. Song, X. Q. Bao and L. F. Liu, *J. Power Sources*, 2016, **330**, 156–166.
83 M. Risch, F. Ringleb, M. Kohlhoff, P. Bogdanoff, P. Chernev, I. Zaharieva and H. Dau, *Energy Environ. Sci.*, 2015, **8**, 661–674.
84 A. L. Ankudinov, B. Ravel, J. J. Rehr and S. D. Conradson, *Phys. Rev. B: Condens. Matter Mater. Phys.*, 1998, **58**, 7565–7576.
85 J. J. Rehr and R. C. Albers, *Rev. Mod. Phys.*, 2000, **72**, 621–654.